

## MIT Open Access Articles

*OFFSHORE WIND TURBINE NONLINEAR  
WAVE LOADS AND THEIR STATISTICS*

The MIT Faculty has made this article openly available. *Please share*  
how this access benefits you. Your story matters.

**As Published:** 10.1115/1.4042264

**Publisher:** ASME International

**Persistent URL:** <https://hdl.handle.net/1721.1/135881>

**Version:** Final published version: final published article, as it appeared in a journal, conference proceedings, or other formally published context

**Terms of Use:** Article is made available in accordance with the publisher's policy and may be subject to US copyright law. Please refer to the publisher's site for terms of use.



## Paul D. Sclavounos

Massachusetts Institute of Technology,  
77 Massachusetts Avenue, 5-320,  
Cambridge, MA 02139  
e-mail: pauls@mit.edu

## Yu Zhang

Massachusetts Institute of Technology,  
77 Massachusetts Avenue, 5-329,  
Cambridge, MA 02139  
e-mail: yu\_zhang@mit.edu

## Yu Ma

Massachusetts Institute of Technology,  
77 Massachusetts Avenue, 5-329,  
Cambridge, MA 02139  
e-mail: yuma@mit.edu

## David F. Larson

Massachusetts Institute of Technology,  
77 Massachusetts Avenue, 5-329,  
Cambridge, MA 02139  
e-mail: dflarson@mit.edu

# Offshore Wind Turbine Nonlinear Wave Loads and Their Statistics

*The development of an analytical model for the prediction of the stochastic nonlinear wave loads on the support structure of bottom mounted and floating offshore wind turbines is presented. Explicit expressions are derived for the time-domain nonlinear exciting forces in a sea state with significant wave height comparable to the diameter of the support structure based on the fluid impulse theory (FIT). The method is validated against experimental measurements with good agreement. The higher order moments of the nonlinear load are evaluated from simulated force records and the derivation of analytical expressions for the nonlinear load statistics for their efficient use in design is addressed. The identification of the inertia and drag coefficients of a generalized nonlinear wave load model trained against experiments using support vector machine learning algorithms is discussed. [DOI: 10.1115/1.4042264]*

## Introduction

The analysis and design of bottom mounted and floating offshore wind turbines requires the development of methods for the evaluation of the environmental loads and their statistics. The majority of the foundations are currently monopiles with truss structures used in deeper waters. The resulting tall structure consisting of the foundation and wind turbine tower structure is subject to stochastic wind and wave loads exciting rigid-body and flexural responses, which must be properly modeled for the development of cost-effective offshore wind turbine systems. These topics represent an active area of research by the offshore wind energy industry at the analytical, computational, and experimental level.

The present paper presents the development of an analytical nonlinear wave load model for monopiles supporting multimegawatt offshore wind turbines in deep and finite water depth. The wavelength corresponding to the modal frequency of design sea states is large compared to the monopile diameter while their significant wave height of 6–10 m is comparable to the diameter of the support structure. Therefore, nonlinear effects must be accounted for in the prediction of the wave loads. The nonlinear wave load model studied in the present paper is based on the fluid impulse theory (FIT) developed in Refs. [1–4]. In the latter reference, an approximation of the exciting force on a vertical cylinder is derived for ambient waves with wavelength large compared to the cylinder diameter and amplitude comparable to its diameter. This model is extended and completed in the present paper. The resulting force expressions are explicit functions of the ambient wave kinematics, which may be provided by linear, second-order theory or by a fully nonlinear wave kinematics model. The derivation is presented with an additional term, which accounts for the enforcement of the second-order free-surface condition. The complete model accounts consistently for all second-order and quadratic effects in waves long compared to the cylinder diameter. Viscous effects are accounted for by the Morison drag term.

The wave load model is validated by simulating the irregular wave exciting forces on the OC5 Spar Buoy and is found to be in very good agreement with experimental measurements. Computations are carried out of the linear, second-order, and viscous wave loads and the nonlinear load components are found to be significant relative to the linear wave load.

The variance, skewness, and kurtosis of the nonlinear wave load are estimated numerically from simulated force records in a sea state with a prescribed spectrum. The skewness is found to be negligible for a nearly symmetric wave load record in deep water. The variance and kurtosis may be readily used for the estimation of the level-crossing rates, extreme and fatigue loads as described in Ref. [5]. Alternatively, the wave load moments may be obtained analytically from the quadratic transfer functions (QTFs), which are available explicitly for the present wave load model using the method in Ref. [6] as implemented in Ref. [7] for the design of a tension leg platform. More generally, the same methodology may be used for the explicit evaluation of the nonlinear load and response statistics of floating offshore wind turbines and offshore platforms at a modest computational effort.

Viscous effects are accounted for by adding a Morison-type drag force term. The inertia and drag coefficients in a generalized form of the present nonlinear wave load model are expected to differ from their corresponding values in the conventional Morison equation where only linear effects are included in the inertia term. The inertia and drag coefficients may be identified from experimental measurements using conventional least squares or support vector machine system identification algorithms.

## Fluid Impulse Theory for a Vertical Cylinder

Figure 1 illustrates a vertical circular cylinder fixed in space, an ambient wave profile, and the calm water level coinciding with the  $z=0$  plane. The positive  $z$ -axis points upward and the unit normal vector points inside the cylinder. The wetted surface under the ambient wave profile is  $S_B(t)$ , the instantaneous ambient wave surface exterior to the cylinder is  $S_f(t)$ , and its portion inside the cylinder is  $S_W(t)$ . The water density is  $\rho$  and the acceleration of gravity is  $g$ .

The fluid impulse theory developed in Ref. [1] expresses the nonlinear surge force on the cylinder, as the sum of the time

Contributed by the Ocean, Offshore, and Arctic Engineering Division of ASME for publication in the JOURNAL OF OFFSHORE MECHANICS AND ARCTIC ENGINEERING. Manuscript received December 26, 2017; final manuscript received September 24, 2018; published online January 22, 2019. Assoc. Editor: Carlos Guedes Soares.

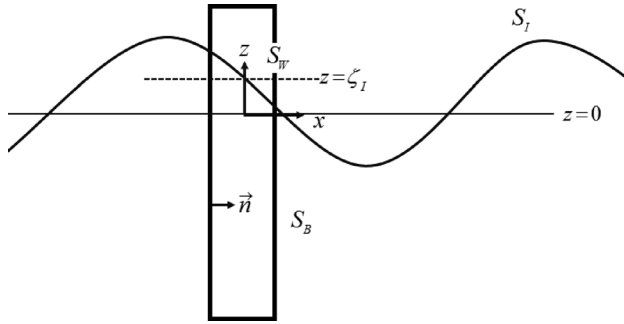


Fig. 1 Schematic of FIT

derivative of Froude–Krylov, diffraction and free-surface impulse components

$$F_X(t) = F_{X,F-K}(t) + F_{X,B}(t) + F_{X,FS}(t)$$

Denote by  $\varphi_I$  and  $\varphi$  the incident and diffraction velocity potentials, respectively. The impulse Froude–Krylov force is given by

$$\begin{aligned} F_{X,F-K}(t) &= -\rho \frac{d}{dt} \left[ \int_{S_B(t)+S_W(t)} \varphi_I n_1 ds \right] \\ &= \rho \frac{d}{dt} \left[ \int_{V_W(t)} \frac{\partial \varphi_I}{\partial x} dv \right] \end{aligned} \quad (1)$$

where Gauss' theorem was invoked. The impulse diffraction force is given by

$$F_{X,B} = -\rho \frac{d}{dt} \left[ \int_{S_B(t)} \varphi n_1 ds \right] \quad (2)$$

The free-surface impulse force in the  $x$ -direction takes the form

$$\begin{aligned} F_{X,FS} &= -\rho \frac{d}{dt} \int_{S_I(t)} \varphi n_1 ds - \rho \frac{d}{dt} \int_{S_I(t)} \frac{\partial \zeta}{\partial x} \frac{\partial \varphi_I}{\partial x} ds \\ &\quad - \rho \frac{d}{dt} \int_{S_I(t)} \zeta \frac{\partial \varphi}{\partial x} ds + O(\varepsilon^3) \end{aligned} \quad (3)$$

where  $\zeta$  is the diffraction wave elevation about the ambient wave profile. Terms of cubic order in the wave steepness  $\varepsilon$  are neglected in Eq. (3). A surface integral over a semispherical surface at infinity involving the inner product of the gradient of the incident and diffraction potentials may be shown to vanish. At a finite time, the diffraction potential at infinity behaves like a three-dimensional dipole and its gradient decays like  $1/R^3$ . This decay offsets the area of the sphere, which grows like  $R^2$ .

It was shown in Ref. [2] that in regular irregular waves with characteristic wavelength large compared to the cylinder diameter, the surge exciting force keeping quadratic terms takes the form (following a correction for a factor of 2 in the last term of Eq. (9) in that paper):

$$\begin{aligned} F_{X,FS}^B &= 2\rho\pi a^2 \int_{-T}^{\zeta_I} \left( \dot{u}_1 + u_1 \frac{\partial u_1}{\partial x} + u_3 \frac{\partial u_1}{\partial z} \right) dz \\ &= -2\pi a^2 \int_{-T}^{\zeta_I} \frac{\partial p_I}{\partial x} dz \end{aligned} \quad (4)$$

In expression (4),  $p_I$  is the incident wave pressure obtained from Euler's equation,  $u_i$  is the ambient wave velocity, and  $\zeta_I(x, t)$  is the ambient wave elevation assumed to be propagating in the positive  $x$ -direction. They may be supplied by linear, second-order theory or a fully nonlinear wave kinematics model.

The derivation of the force expression (4) is based on the assumption that the disturbance potential  $\varphi^{(1)}$  in the impulse

diffraction force (2) satisfies the linearized free-surface condition on a horizontal plane intersecting the cylinder at an elevation  $z = \zeta_I(0, t)$ . In order to account for all second-order effects in the fluid impulse force (4), the contribution of the second-order disturbance potential  $\varphi^{(2)}$  must also be added to the diffraction force component (2). This second-order potential satisfies the homogeneous normal velocity condition on the cylinder boundary and the inhomogeneous free-surface condition

$$\begin{aligned} \frac{\partial \varphi^{(2)}}{\partial n} &= 0, \quad S_B \\ \frac{\partial^2 \varphi^{(2)}}{\partial t^2} + g \frac{\partial \varphi^{(2)}}{\partial z} &= -2 \frac{\partial}{\partial t} \left[ \nabla \varphi_I \cdot \nabla \varphi^{(1)} \right], \quad z = \zeta_I \end{aligned} \quad (5)$$

The forcing term in the right-hand side of the free-surface condition includes the inner product of gradients of the incident and linear disturbance potentials. The inner product of the gradients of the incident wave potential is accounted for by the nonlinear ambient wave kinematics model and the inner product of the gradients of the linear disturbance potential is of higher order for wavelengths large compared to the cylinder diameter.

The velocity potential satisfying the inhomogeneous boundary value problem (5) is decomposed into two potentials satisfying the following boundary-value problems:

$$\begin{aligned} \varphi^{(2)} &= \psi + \chi \\ \frac{\partial^2 \psi}{\partial t^2} + g \frac{\partial \psi}{\partial z} &= -2 \frac{\partial}{\partial t} \left[ \nabla \varphi_I \cdot \nabla \varphi^{(1)} \right], \quad z = 0 \\ \frac{\partial^2 \chi}{\partial t^2} + g \frac{\partial \chi}{\partial z} &= 0, \quad z = 0 \\ \frac{\partial \chi}{\partial n} &= -\frac{\partial \psi}{\partial n}, \quad S_{\text{body, bottom}} \end{aligned} \quad (6)$$

The potential  $\psi$  satisfies the Laplace equation in the fluid domain and the inhomogeneous free-surface condition in an otherwise open lower fluid domain, which does not include the body boundary. It may be considered as an "incident second-order flow potential." The scattering potential  $\chi$  satisfies the homogeneous free-surface condition and on the body boundary, it offsets the normal velocity due to the potential  $\psi$ . Their sum may be easily verified to satisfy the boundary value problem (5).

The velocity potential  $\psi$  may be obtained explicitly in the form [8, eq. (22.48)]

$$\begin{aligned} \psi(x, y, z, t) &= \frac{1}{2\pi} \iint_{z=0} d\zeta d\eta \int_0^t d\tau f(\zeta, \eta, \tau) \int_0^\infty dk \kappa(z, \tau, k) \\ R^2 &= (x - \zeta)^2 + (y - \eta)^2 \\ f(\zeta, \eta, \tau) &= -2 \frac{\partial}{\partial t} \left[ \nabla \varphi_I \cdot \nabla \varphi^{(1)} \right] \\ \kappa(z, \tau, k) &= k e^{kz} \frac{\sin[\sqrt{gk}(t - \tau)]}{\sqrt{gk}} J_0(kR) \end{aligned} \quad (7)$$

where  $R$  is the horizontal distance between source point and field point. In ambient waves, long compared to the cylinder diameter, the leading-order sectional force exerted on the cylinder due to the flow represented by the potential  $\psi$  is proportional to the respective pressure gradient multiplied by  $2\pi a^2$  by virtue of G. I. Taylor's theorem for a slowly varying inflow. Therefore, the quantity of interest is the negative of the pressure gradient on the axis of the cylinder, or  $\rho(\partial/\partial t)(\partial\psi/\partial x)(0, 0, z)$ . The second-order force follows upon integration of the pressure gradient over the cylinder draft multiplied by  $2\pi a^2$ :

Introduce the polar coordinates

$$\begin{aligned} x &= R_\xi \cos \theta_\xi; & y &= R_\xi \sin \theta_\xi \\ \xi &= R_\xi \cos \theta_\xi; & \eta &= R_\xi \sin \theta_\xi \end{aligned} \quad (8)$$

Taking the time and  $x$ -derivative of expression (7), converting into polar coordinates and evaluating the result on the  $x, y = 0$  axis, it follows that:

$$\begin{aligned} \frac{\partial^2 \psi(0, 0, z, t)}{\partial x \partial t} &= -\frac{1}{\pi} \int_a^\infty dR_\xi R_\xi \int_0^\infty d\theta_\xi \alpha(R_\xi, \theta_\xi) \int_0^\infty dk \beta(R_\xi, z) \\ &\quad - \frac{1}{\pi} \int_0^t d\tau \int_a^\infty dR_\xi R_\xi \int_0^\infty d\theta_\xi \alpha(R_\xi, \theta_\xi) \\ &\quad \times \int_0^\infty dk \beta(R_\xi, z) \sin[\sqrt{gk}(t-\tau)] \\ \alpha(R_\xi, \theta_\xi) &= \cos \theta_\xi [\nabla \phi_I \cdot \nabla \phi^{(1)}](R_\xi, \theta_\xi) \\ \beta(R_\xi, z) &= k^2 e^{kz} J_1(kR_\xi) \end{aligned} \quad (9)$$

The first term in the right-hand side of Eq. (9) represents the time-local contribution while the time-convolution integral represents the memory effect. In long waves  $((\lambda/D) \gg 15)$ , the time-local term represents the leading-order contribution as is the case with the linear inertial load in the conventional Morison equation. To leading order in long incident waves, the slender body approximation of the linear diffraction potential is invoked to obtain on  $z = 0$  and in unidirectional waves

$$\begin{aligned} \phi^{(1)}(R, \theta, z) &= -u_1(z) \frac{a^2}{R} \cos \theta \\ \nabla \phi_I \cdot \nabla \phi^{(1)} &= \frac{\partial \phi_I}{\partial z} \frac{\partial \phi^{(1)}}{\partial z} + \frac{\partial \phi_I}{\partial x} \frac{\partial \phi^{(1)}}{\partial x} \\ &= \frac{\partial \phi_I}{\partial z} \frac{\partial \phi^{(1)}}{\partial z} + u_1 \left( \cos \theta \frac{\partial \phi^{(1)}}{\partial R} - \frac{\sin \theta}{R} \frac{\partial \phi^{(1)}}{\partial \theta} \right) \\ &= \frac{\partial \phi_I}{\partial z} \frac{\partial u_1}{\partial z} \left( -\frac{a^2}{R} \cos \theta \right) + \frac{u_1^2 a^2}{R^2} (\cos^2 \theta - \sin^2 \theta), \quad z = 0 \end{aligned} \quad (10)$$

In Eq. (10), the leading-order linear disturbance potential  $\phi^{(1)}$  is a dipole-like disturbance around a circle with radius  $a$ . The inflow velocity  $u_1$  in the  $x$ -direction is equal to that of the ambient wave evaluated on the cylinder axis.

Upon substitution of Eq. (10) in the first term of Eq. (9), the last term in Eq. (10) vanishes identically upon integration in the  $\theta$ -direction. It follows that:

$$\begin{aligned} \frac{\partial^2 \psi(0, 0, z, t)}{\partial x \partial t} &= \frac{\partial \phi_I(0, 0, 0)}{\partial z} \frac{\partial u_1(0, 0, 0)}{\partial z} \frac{a^2}{\pi} \int_a^\infty dR \int_0^{2\pi} d\theta \cos^2 \theta \\ &\quad \times \int_0^\infty dk \beta(R_\xi, z) \end{aligned} \quad (11)$$

Invoking the kinematic free-surface condition satisfied by the incident wave potential at the origin of the coordinate system, we obtain

$$\begin{aligned} \frac{\partial \phi_I(0, 0, 0)}{\partial z} &= \frac{\partial \zeta_I}{\partial t} \\ \frac{\partial u_1(0, 0, 0)}{\partial z} &= \frac{\partial}{\partial z} \left( \frac{\partial \phi_I}{\partial x} \right) = \frac{\partial}{\partial x} \left( \frac{\partial \phi_I}{\partial z} \right) = \frac{\partial}{\partial x} \left( \frac{\partial \zeta_I}{\partial t} \right) \end{aligned} \quad (12)$$

The force follows upon substitution of the flow acceleration (11) in G. I. Taylor's theorem and integration in the  $z$ -direction assuming a cylinder of large draft. Multiplying by  $2\pi\rho a^2$  and upon the explicit evaluation of the integrals in Eq. (11), the force contribution due to the second-order disturbance potential takes the form

$$F_2 = 2\pi\rho a^2 \left( \frac{a}{2} \right) \frac{\partial}{\partial x} \left( \frac{\partial \zeta_I}{\partial t} \right)^2 \quad (13)$$

The total fluid impulse wave load follows from expressions (4) and (13) in the form:

$$\begin{aligned} F_X &= 2\pi\rho a^2 \left\{ \int_{-T}^{\zeta_I} \left( \dot{u}_1^{(1)} + \dot{u}_1^{(2)} + u_1 \frac{\partial u_1}{\partial x} + u_3 \frac{\partial u_1}{\partial z} \right) dz \right. \\ &\quad \left. + \frac{a}{2} \frac{\partial}{\partial x} \left( \frac{\partial \zeta_I}{\partial t} \right)^2 \right\}_{x=0, z=0} \end{aligned} \quad (14)$$

The second-order contribution to the horizontal acceleration of the ambient wave was also included in Eq. (14). This force expression applies in deep water. It may be easily extended in water of finite depth by invoking the corresponding definitions of the linear and second-order incident wave velocity potential. The value of the  $C_m$  coefficient is assumed to be equal to 2 in Eq. (14). This assumption is relaxed later when the viscous drag term is added and the identification of the  $C_m$  and  $C_d$  coefficients from experiments is discussed.

### Fluid Impulse Theory's Verification With Panel Method

The fluid impulse theory's linear wave load model  $F_X = 2\pi\rho a^2 \int_{-T}^0 \dot{u}_1^{(1)} dz$  is verified against WAMIT [9]. As shown in Fig. 2 below, FIT linear model and WAMIT are in very good agreement, the variance of FIT linear model is  $1.0812 \times 10^{12}$ , and the variance of WAMIT model is  $1.0756 \times 10^{12}$ , which indicates that the FIT linear model is a good approximation of linear wave load under the long wave assumption, and all nonlinearities arise from higher order effects instead of finite  $ka$  effects.

### Fluid Impulse Theory's Validation With Experiment

The fluid impulse nonlinear wave load was validated by the experimental results from the offshore code comparison collaboration continuation, with correlation project (OC5) [10]. Single steel cylinders with diameter of 0.2 m and draft of 1.44 m were tested. The bottom surface of the cylinder is flat and the upper surface pierces the still water line. Force transducers recorded the load along the wave propagation direction, with a sufficiently stiff frame to warrant modeling the cylinder as fixed and rigid. The irregular wave test was run for a duration of 1700 s, with a significant wave height of 0.357 m and a peak period of 2.76 s. The experiments use a water depth sufficiently large such that they can be considered to occur in deep water conditions. The simulations

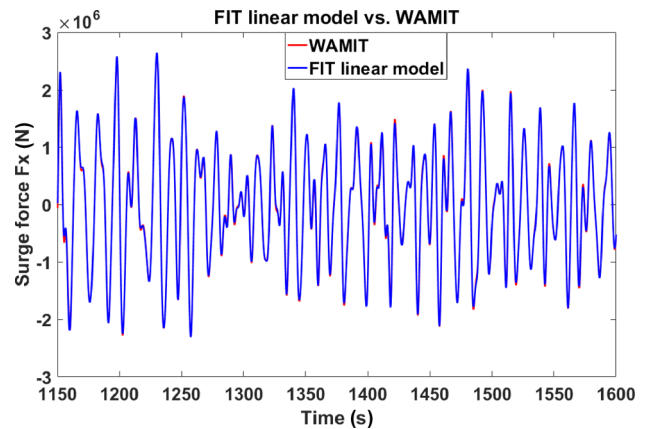
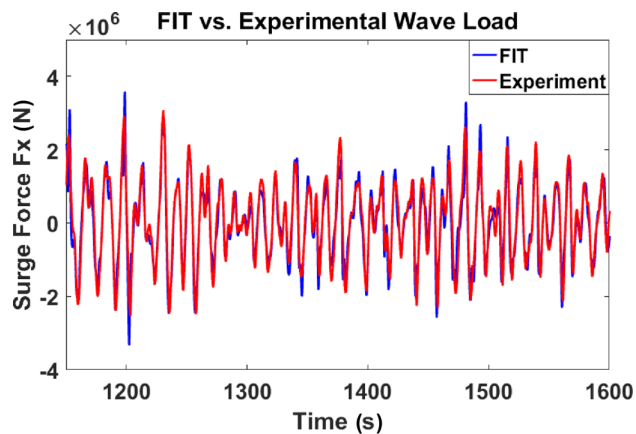


Fig. 2 FIT linear model verification with WAMIT's results

**Table 1 Parameters in experiment and simulation**

	Diameter (m)	Draft (m)	$H_s$ (m)	$T_p$ (s)
Model scale	0.2	1.44	0.357	2.76
Full scale	6	43.2	10.71	15

**Fig. 3 FIT full model validation with experimental wave loads**

reported in this paper refer to the full-scale data instead of the model scale data (scale ratio = 30) (Table 1).

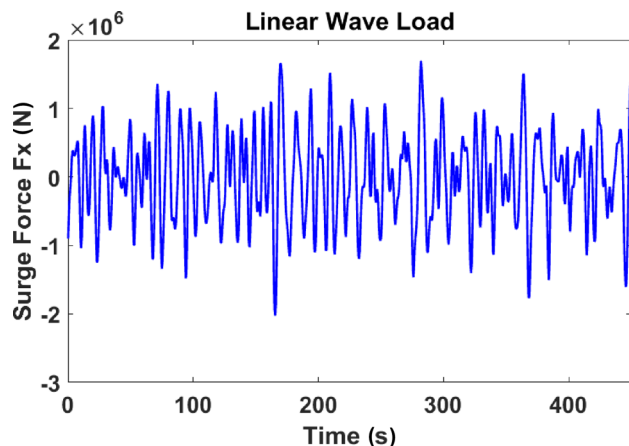
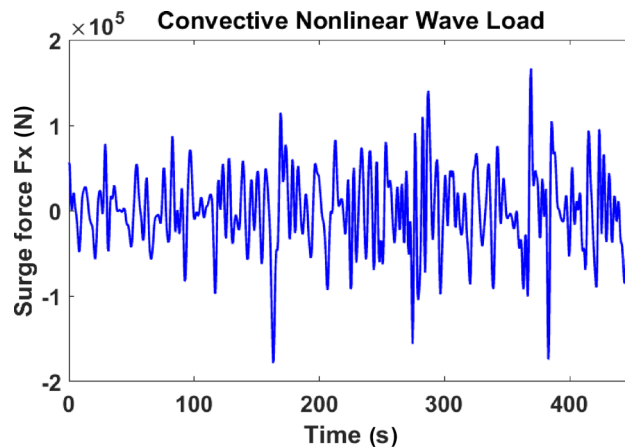
Each simulation lasts 450 s with a time-step of 0.1 s. For consistency between the simulations and experiments, the irregular wave parameters are obtained by a Fourier transform of the experimental wave elevation measurements. The amplitudes and phases of the irregular waves are extracted from the experiment and supplied as input to the simulation. The comparison is shown below:

A good agreement is found between the fluid impulse theory model (14) and the experimental results. The variance of the FIT model is  $1.2321 \times 10^{12}$ , and the variance of experimental results is  $1.1856 \times 10^{12}$ , and they are within a 4% error. The possible reason about the difference might be the higher order nonlinearities in experiments (Fig. 3).

### Comparison of Linear and Quadratic Wave Loads

The linear and quadratic components are studied separately in this section. A 450 s simulation of a cylinder subject to an irregular wave sea state with  $H_s = 10$  m and  $T_p = 15$  s in deep water is used as an example. The frequency increment is  $\Delta\omega = 0.005$  rad/s. The cylinder has a diameter of 6 m and a draft of 20 m.

The linear wave load component (Fig. 4) is

**Fig. 4 Linear wave load****Fig. 5 Nonlinear wave load (convective term)**

$$F_X^{(1)} = 2\pi\rho a^2 \int_{-T}^0 \dot{u}_1 dz$$

The nonlinear wave load due to the convective terms in the fluid acceleration is (Fig. 5)

$$F_X^{(2)} = 2\pi\rho a^2 \int_{-T}^0 \left( u_1 \frac{\partial u_1}{\partial x} + u_3 \frac{\partial u_1}{\partial z} \right) dz$$

The nonlinear wave load due to the waterline quadratic contribution is (Fig. 6)

$$F_X^{(3)} = 2\pi\rho a^2 \dot{u}_1 \zeta_l$$

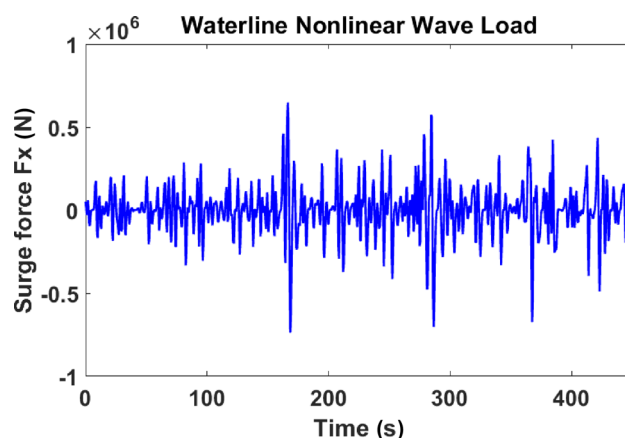
The nonlinear wave load due to the second-order disturbance velocity potential effect is (Fig. 7)

$$F_X^{(4)} = \pi\rho a^3 \frac{\partial}{\partial x} \left( \frac{\partial \zeta_l}{\partial t} \right)_{x=0, z=0}$$

The nonlinear wave load due to second-order incident potential effect is (Fig. 8)

$$F_X^{(5)} = 2\pi\rho a^2 \int_{-T}^0 \dot{u}_1^{(2)} dz$$

The nonlinear force components  $F_X^{(2)}$ ,  $F_X^{(3)}$ ,  $F_X^{(4)}$ , and  $F_X^{(5)}$  are defined in Eq. (14).

**Fig. 6 Nonlinear wave load (waterline term)**



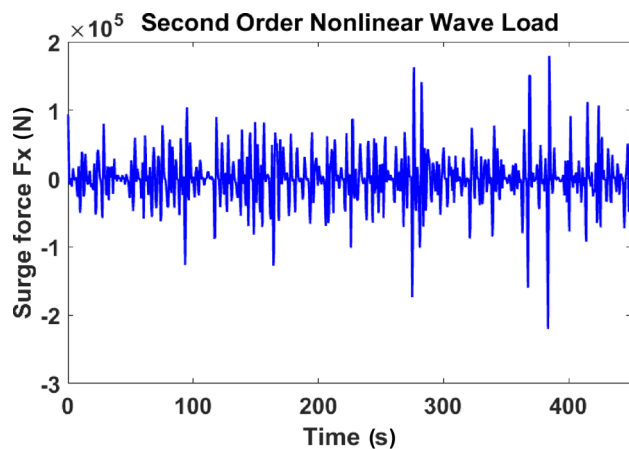


Fig. 7 Nonlinear wave load (second-order disturbance potential term)

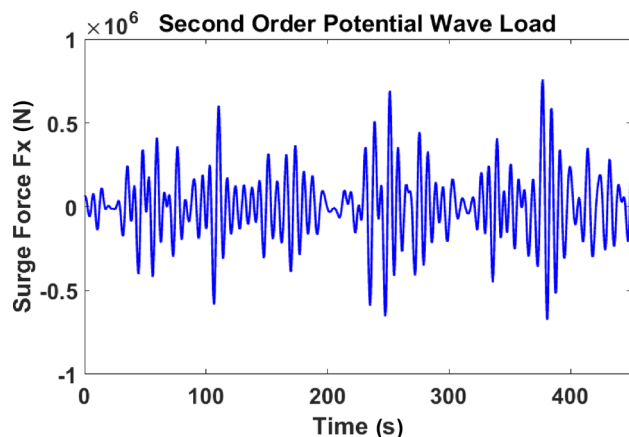


Fig. 8 Nonlinear wave load (second-order incident potential term)

#### Viscous Effects

The viscous force (Fig. 9) is estimated by applying Morison's equation

$$F_{\text{viscous}} = \frac{1}{2} \rho \cdot 2a \cdot C_D \int_{-T}^0 u_1 |u_1| dz$$

Where  $C_D$  is the viscous drag coefficient, set equal to 0.7.

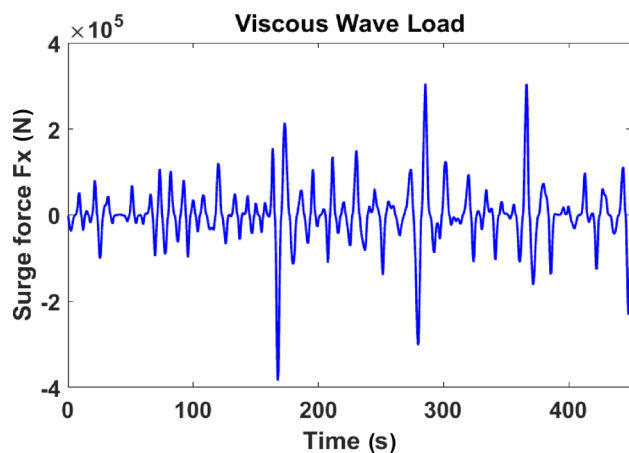
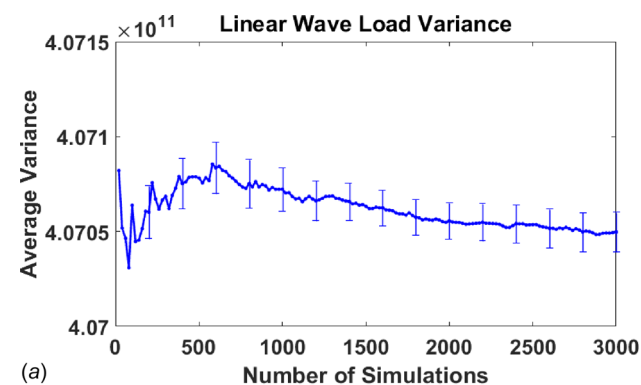


Fig. 9 Viscous wave load

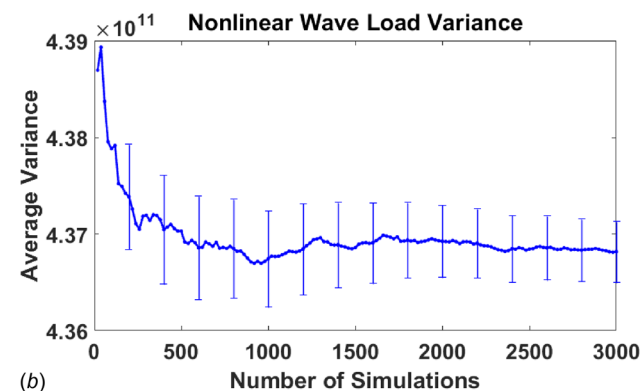
#### Nonlinear Wave Load Statistics

The nonlinear statistics of interest are the wave load variance and kurtosis. In order to obtain convergent estimates of the load moments, a total of up to 6000 simulations were carried out, each lasting 1257 s. The simulations were carried out for a spectrum bandwidth of (0, 2.5) rad/s, discretized using a frequency increment  $\Delta\omega = 0.005$  rad/s corresponding to a signal periodicity of 1257 s.

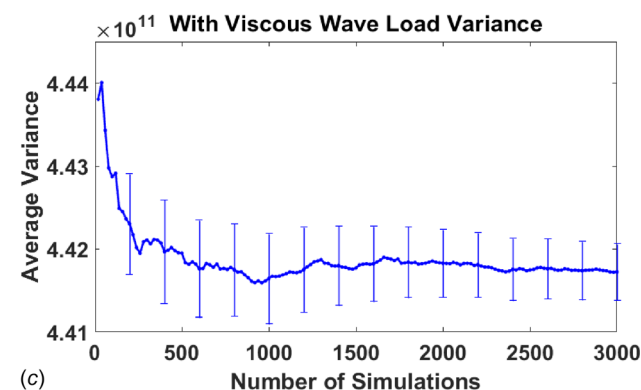
Figure 10 illustrates the convergence of the estimates of the variance of the linear, and linear plus nonlinear load, the latter also including the viscous force. The estimates are obtained by averaging a large number of independent simulations. The variance estimates are convergent within a small error band, indicated in the figures. The nonlinear load variance is found to be 8.5% larger than the linear variance, and the nonlinear load variance is found to be very close to the experimental variance within a 4% error. The nonlinear wave load component  $F_X^{(5)}$  due to the second-order effect in the ambient wave horizontal acceleration was not included in the simulations presented in Fig. 10 and is discussed separately below in Figs. 11 and 12.



(a)



(b)



(c)

Fig. 10 Variance of the linear (a), linear + nonlinear (b), and linear + nonlinear + viscous (c) wave load

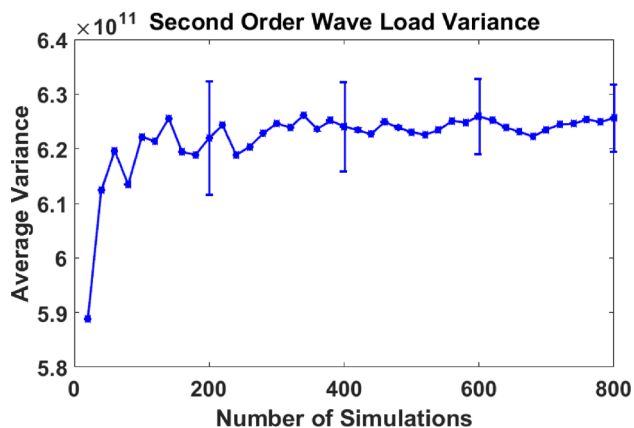


Fig. 11 Variance of the nonlinear wave load including second-order incident wave effect

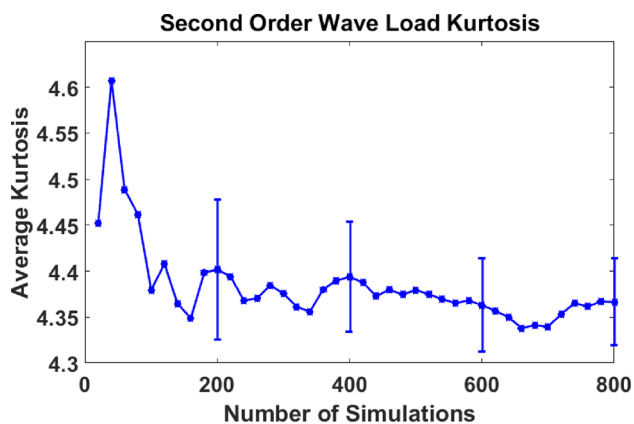


Fig. 12 Kurtosis of the nonlinear wave load including second-order incident wave effect

Figure 13 illustrates the convergence of the estimates of the linear and nonlinear load kurtosis. As expected, the linear load kurtosis converges to the value of three for a Gaussian signal. The kurtosis of the linear plus nonlinear load is estimated to be 3.7, 23% larger than that of the linear load. The estimation of the kurtosis converges to within a small error band, indicated in the figure. The wave load component  $F_X^{(5)}$  due to the second-order effect in the ambient wave horizontal acceleration was not included in the simulations presented in Fig. 13 and is discussed separately below.

Figure 11 plots the variance of the nonlinear wave load including the effect of the second-order potential in the evaluation of the ambient wave particle acceleration in expression (14). A comparison with the variance plotted in Fig. 10 where the second-order ambient wave effect was not included indicates that the second-order incident wave effect increases the variance by 40%. Figure 12 plots the kurtosis of the nonlinear wave load again accounting for the second-order ambient wave effect. A comparison with the results of Fig. 13 indicates that the second-order incident wave effect increases the kurtosis of the nonlinear wave load by 18%. Moreover, the total kurtosis of the complete nonlinear wave load model is 4.38 or 46% larger than the kurtosis of three of the linear Gaussian inertial wave load present in the conventional Morison equation. The viscous drag force was found to have a smaller effect on the variance and kurtosis relative to that of the nonlinear inertial wave load components. The magnitude of the skewness was found to be very small due to the symmetry of the wave load record. This is, however, not expected to be the case in shallow water, and this will be the topic of a future study.

The simulations presented in the present section suggest that accounting for all quadratic wave effects in the wave load (14)

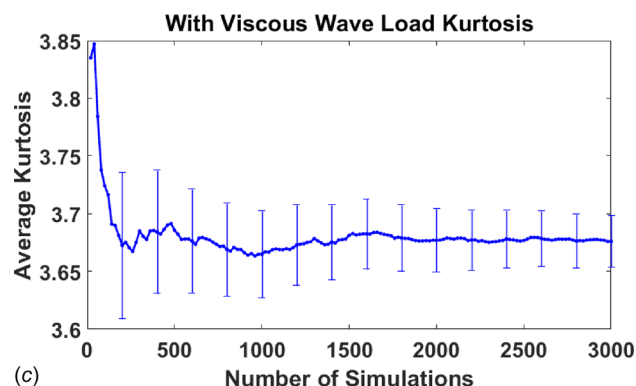
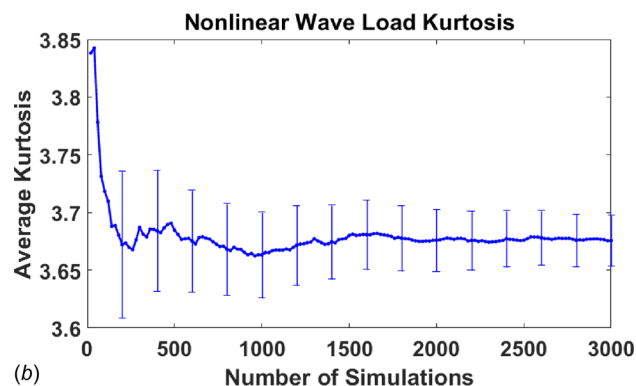
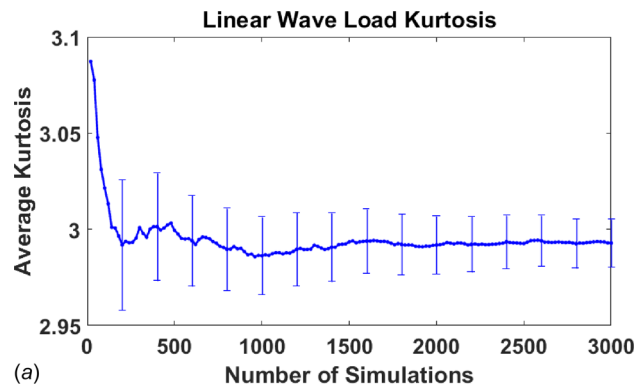


Fig. 13 Kurtosis of the linear (a), linear + nonlinear (b), and linear + nonlinear + viscous (c) wave load

derived from the fluid impulse theory contributes significant nonlinearities to the force statistics. These effects must be accounted for in the evaluation of the level-crossing rates, extreme and fatigue loads as discussed in Ref. [11]. The computational effort necessary to obtain the load moments presented in Figs. 10–13 is considerable even for the analytical wave load model (14) and the convergence rate with increasing number of samples is rather slow. Therefore, the derivation of analytical methods for the evaluation of the higher order load moments is desirable and is discussed in the conclusions section.

### Nonlinear Wave Load and Moment in Finite Water Depth

Computations were carried out of the nonlinear wave loads predicted by FIT on an offshore wind turbine tower in shallow water where the nonlinearity of the wave loads is more pronounced.

Figure 14 plots the horizontal load in a water depth of 19 m and in a sea state with  $H_s = 6$  m and  $T_p = 10$  s. Figure 15 plots the corresponding moment at the mudline. The moment in FIT was evaluated by multiplying the sectional loads by their vertical distance

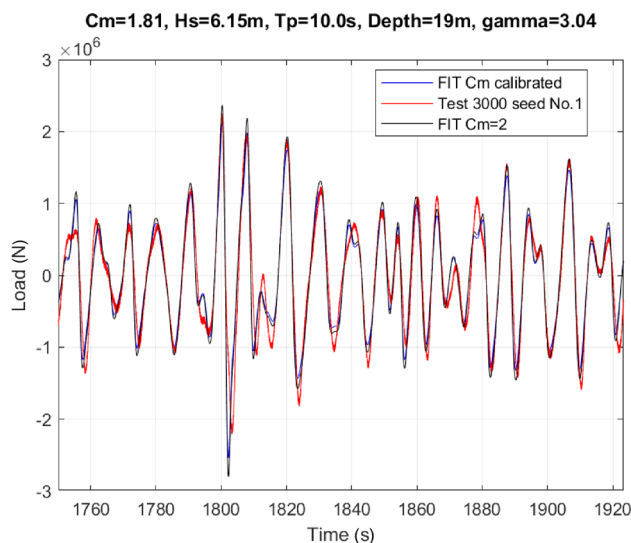


Fig. 14 Nonlinear horizontal load in finite water depth

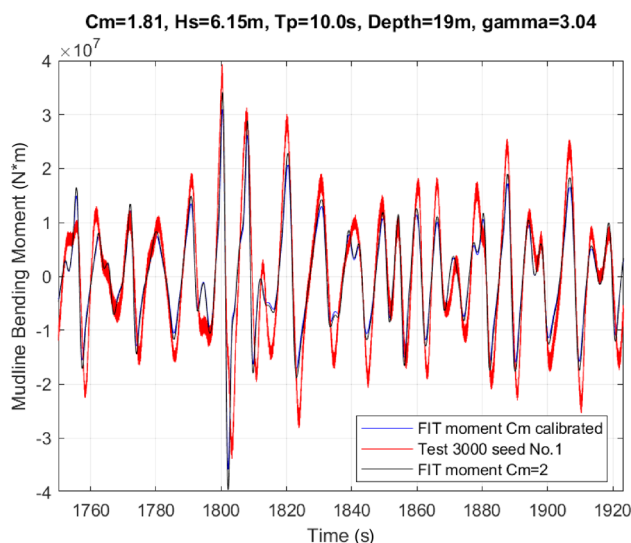


Fig. 15 Nonlinear mudline bending moment in finite water depth

from the mudline. The force and moment records are compared to tank experimental measurements in Figs. 14 and 15 with good agreement.

In Figs. 14 and 15, the value of the  $C_m$  coefficient used in FIT was set equal to the theoretical value of 2 and to the calibrated value of 1.81, which minimizes the mean square error of the FIT predictions relative to the experimental measurements.

### Level-Crossing Rates of Nonlinear Bending Moment

While the agreement between the simulated FIT linear and quadratic load and moment in deep and finite water depth looks good, discrepancies are visible near the peaks. These discrepancies are studied in more detail next by evaluating the level-crossing rates of the mudline bending moment.

The skewness and kurtosis of the bending moment were evaluated from the FIT simulations and used with the method described in Ref. [5] to estimate the level-crossing rates as a function of the ratio of the bending moment divided by its standard deviation. A significant discrepancy of the probability of exceedance is evident for a bending moment to standard deviation ratio

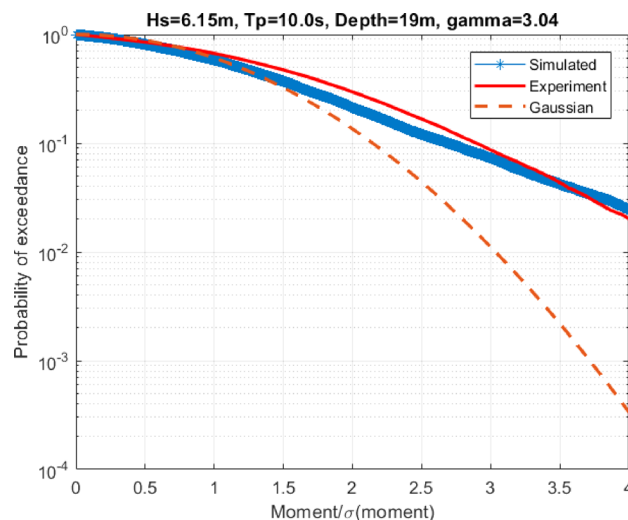


Fig. 16 Bending moment probability of exceedance. Fit versus experiment versus linear theory.

greater than 1.5. Therefore, quadratic nonlinear effects accounted for by FIT lead to a marked increase of the probability of exceedance of the bending moment relative to the predictions of linear theory.

The probability of exceedance predicted by FIT is also compared to the corresponding exceedance rates obtained from the experimental measurements in Fig. 16. The FIT model successfully captures most of nonlinearities in the experiment, while there are still some discrepancies between FIT model and experimental measurements. The FIT wave load model accounts for quadratic wave nonlinearities and in the present simulations, viscous effects were not accounted for. The impact of higher order nonlinearities and viscous flow separation in the vicinity of the waterline may impact the exceedance rates. The significance of these effects might be the reason for the discrepancies between FIT model exceedance rate and the experimental exceedance rate.

The modeling of such strong flow nonlinearities is discussed in the Analytical Stochastic Models. Machine Learning of Strong Nonlinearities section.

### Analytical Stochastic Models. Machine Learning of Strong Nonlinearities

The compact form of the quadratic wave load given by expression (14) allows the derivation of explicit expressions for the sum- and difference-frequency quadratic force transfer functions in deep and finite water depth in unidirectional and directional seas. The quadratic force is an explicit function of the ambient wave kinematics and the linear and second-order velocity potentials of bichromatic and bidirectional plane progressive waves are available in closed form. Given an ambient wave spectrum discretized over a frequency band that overlaps with the natural frequencies of the first few flexural modes of the offshore wind turbine, the linear and quadratic wave load may be cast as the sum of a linear and quadratic time series involving independent Gaussian random variates functions of the amplitudes of the ambient sea state as discussed in Ref. [7]. A singular value decomposition of the resulting quadratic form involving the second-order QTFs leads to the representation of the nonlinear component of the wave load as the sum of squares of Gaussian random variables with explicit distributions. This representation allows the derivation of analytical expressions for the variance, skewness, and kurtosis of the nonlinear load leading to a significant reduction of the computational effort relative to direct simulations. This is of considerable practical interest since the analysis and design of offshore wind turbine



systems must be carried out in directional seas and multiple wind and wave environmental conditions.

The validation of the components of the nonlinear wave load model developed in the current paper may be carried out by a comparison with the exact QTFs evaluated by WAMIT<sup>TM</sup>, the use of a fully nonlinear potential flow method that accounts for the exact ambient wave kinematics, computational fluid dynamics simulations, which account both for strong free-surface nonlinearities and viscous diffraction effects and experiments.

Viscous effects in the present model may be accounted for by using Morison's equation with an appropriate value for the drag coefficient  $C_d$ . The proper specification of the  $C_m$  coefficient in Eq. (14) is also necessary, which, in the present paper, was set equal to 2. A generalization of the nonlinear force model derived in the present paper may account for the interaction of potential and viscous flow effects, wave memory effects, and strong free-surface nonlinearities by introducing inertia and drag coefficients  $C_{m1}$ ,  $C_{m2}$ , and  $C_d$  as follows:

$$F_X = \pi \rho a^2 C_{m1} \int_{-T}^{\zeta_l} \left( \dot{u}_1^{(1)} + \dot{u}_1^{(2)} + u_1 \frac{\partial u_1}{\partial x} + u_3 \frac{\partial u_1}{\partial z} \right) dz + C_{m2} \frac{\pi \rho a^3}{2} \frac{\partial}{\partial x} \left( \frac{\partial \zeta_l}{\partial t} \right)^2_{x,z=0} + \rho a C_D \int_{-T}^0 u_1 |u_1| dz \quad (15)$$

The flow physics included in Eq. (15) accounts for linear, second-order, and quadratic nonlinearities in the inertia force component, a separate inertia coefficient for the body and waterline force, and a Morison-type viscous drag force. The values of the body and waterline inertial coefficients  $C_{m1}$ ,  $C_{m2}$ , and drag coefficient  $C_d$  in Eq. (15) account for coupling between ideal and viscous effects, memory effects, and strong free-surface nonlinearities. Their values will depend on the Reynolds, KC numbers, and the parameters of the ambient sea state. Moreover, they will differ from their values in the conventional Morison model, which does not account for quadratic and waterline wave load effects.

The optimal values of  $C_{m1}$ ,  $C_{m2}$ , and  $C_d$  may be determined from experimental measurements of the ambient wave kinematics and the forces on the OC5 Spar. This task may be carried out by least-squares fitting of the force expression given by Eq. (15) to experimental measurements and estimation the three unknown coefficients. More generally, system identification support vector machine learning algorithms may be used for the identification of  $C_{m1}$ ,  $C_{m2}$ , and  $C_d$ . SVM-SI learning methods have been shown to perform very well with short training records and have proven very effective in identifying the inertial and viscous hydrodynamic derivatives of linear and nonlinear ship maneuvering models [12,13], which also account for coupled inertia and separated viscous flow physics. Moreover, the satisfactory performance of

SVM learning algorithms has been validated in a wide range of disciplines. The use of SI-SVM algorithms with the generalized wave load model (15) and its extensions trained against experimental measurements, the optimal estimation of the associated body and waterline potential flow inertia, and viscous drag coefficients in a sea state will be the subject of a future study.

## Acknowledgment

This research was supported by Statoil as part of the MIT-NTNU collaboration program of the MIT Energy Initiative. This financial support is gratefully acknowledged.

## Funding Data

- Statoil (MIT-NTNU collaborate).

## References

- [1] Slavounos, P. D., 2012, "Nonlinear Impulse of Ocean Waves on Floating Bodies," *J. Fluid Mech.*, **697**, pp. 316–335.
- [2] Slavounos, P. D., 2016, "Nonlinear Loads on a Vertical Circular Cylinder," 31st International Workshop on Water Waves and Floating Bodies, Plymouth, MI, Apr. 3–6, pp. 153–156.
- [3] Zhang, Y., 2015, "Wave Loads on Offshore Wind Turbines," *M.S. thesis*, Massachusetts Institute of Technology, Cambridge, MA.
- [4] Slavounos, P. D., Zhang, Y., Ma, Y., and Larson, D. F., "Offshore Wind Turbine Nonlinear Wave Loads and Their Statistics," *ASME Paper No. OMAE2017-61184*.
- [5] Winterstein, S. R., and MacKenzie, C. A., 2013, "Extremes of Nonlinear Vibration: Comparing Models Based on Moments, L-Moments and Maximum Entropy," *ASME J. Offshore Mech. Arct. Eng.*, **135**(2), p. 021602.
- [6] Kac, M., and Siegert, A. J. F., 1947, "On the Theory of Noise in Radio Receivers With Square Law Detectors," *J. Appl. Phys.*, **18**(4), pp. 383–400.
- [7] Winterstein, S. R., Ude, T. C., and Kleiven, G., 1994, "Springing and Slow-Drift Responses: Predicted Extremes and Fatigue vs. Simulation," *BOSS-94 Conference*, Cambridge MA, pp. 1–15.
- [8] Wehausen, J., and Laitone, E., 1960, "Surface Waves," *Fluid Dynamics/Strömungsmechanik*, Springer, Berlin, pp. 446–778.
- [9] Lee, C.-H., 1995, "WAMIT Theory Manual," Massachusetts Institute of Technology, Cambridge, MA.
- [10] Robertson, A. N., Wendt, F. F., Jonkman, J. M., Popko, W., Vorpahl, F., Stansberg, C. T., Bachynski, E. E., Bayati, I., Beyer, F., de Vaal, J. B., and Harries, R., 2015, "OC5 Project Phase I: Validation of Hydrodynamic Loading on a Fixed Cylinder," *25th International Offshore and Polar Engineering Conference. International Society of Offshore and Polar Engineers*, Kona, HI, June 21–26.
- [11] Naess, A., and Moan, T., 2013, *Stochastic Dynamics of Marine Structures*, Cambridge University Press, Cambridge, UK.
- [12] Moreno-Salinas, D., Chaos, D., de la Cruz, J. M., and Aranda, J., 2013, "Identification of a Surface Marine Vessel Using LS-SVM," *J. Appl. Math.*, **2013**, p. 803648.
- [13] Luo, W., Soares, C. G., and Zou, Z., 2016, "Parameter Identification of Ship Maneuvering Model Based on Support Vector Machines and Particle Swarm Optimization," *ASME J. Offshore Mech. Arct. Eng.*, **138**(3), p. 031101.